All-optical switching using optical bistability in non-linear photonic crystals

Marin Soljačić[(a)], Mihai Ibanescu[(a)], Chiyan Luo[(a)], Steven G. Johnson[(a)], Shanhui Fan[(c)], Yoel Fink[(b)], and J.D.Joannopoulos[(a)]

(a) Department of Physics, MIT; Cambridge, MA 02139
(b) Department of Material Science and Engineering, MIT; Cambridge, MA 02139
(c) Department of El. Eng., Stanford University, Palo Alto, CA 94304

ABSTRACT

We demonstrate optical bistability in a class of non-linear photonic crystal devices, through the use of detailed numerical experiments, and analytical theory. Our devices are shorter than the wavelength of light in length, they can operate with only a few mW of power, and can be faster than 1ps.

1. INTRODUCTION

A powerful principle that could be explored to implement all-optical transistors, switches, logical gates, and memory, is the concept of optical bistability. In systems that display optical bistability, the outgoing intensity is a strongly non-linear function of the input intensity, and might even display a hysteresis loop. We present a few photonic crystal devices demonstrating optical bistability. The use of photonic crystals enables the system to be on the order of the wavelength of light, consume only a few *mW* of power, and have a recovery and response time smaller than *1ps*. In Section 2, we present single-defect photonic crystal systems that exhibit optical bistability. In Section 3, we present bistability in axially modulated OmniGuide photonic crystal fibers. In Section 4, we demonstrate optical bistability in double-defect photonic crystal systems. We conclude in Section 5.

2. BISTABILITY IN SINGLE-DEFECT PHOTONIC CRYSTAL SYSTEMS

In this Section, we use the flexibility offered by photonic crystals [1,2,3] to design a system that is effectively one-dimensional, although it is embedded in a higher-dimensional world. Because our system is one-dimensional and single mode, it differs from previous studies [4,5,6] and provides optimal control over input and output. For example, one can achieve 100% peak theoretical transmission. As a consequence, the system is particularly suitable for large-scale all-optical integration. We solve the full non-linear Maxwell's equations numerically (with minimal physical approximations) to demonstrate optical bistability in this system. We also develop an analytical model that excellently describes the behavior of the system and is very useful in predicting and elucidating bistability phenomena.

Photonic Crystal Materials and Devices, Ali Adibi, Axel Scherer, Shawn Yu Lin, Editors,
Proceedings of SPIE Vol. 5000 (2003) © 2003 SPIE · 0277-786X/03/$15.00

Ideally, we would like to work with a 3D photonic crystal system. Recently, however, a 3D photonic crystal structure has been introduced that can closely emulate the photonic state frequencies and field patterns of 2D photonic crystal systems [7]. In particular, cross sections of point and line-defect modes in that structure are very similar to the profiles of the modes we describe in the present manuscript. We can therefore simplify our calculations without loss of generality by constructing the system in 2D. Our design is shown in Figure 1. It resides in a square lattice 2D PC of high-n dielectric rods *(n_H=3.5)* embedded in a low-n dielectric material *(n_L=1.5).* The lattice spacing is denoted by *a*, and the radius of each rod is *r=a/4*. We focus attention on transverse-magnetic (TM) modes, which have electric field parallel to the rods. To create single-mode waveguides (line defects) inside of this PC, we reduce the radius of each rod in a line to *r/3*[(*)]. Further, we also create a resonant cavity (point defect) that supports a dipole-type localized resonant mode by increasing the radius of a single rod to *5r/3*. We connect this cavity with the outside world by placing it *3* unperturbed rods away from the two waveguides, one of the waveguides serving as the input port to the cavity and the other serving as the output port. The cavity couples to the two ports through tunneling processes. It is important for optimal transmission that the cavity be identically coupled to the input and output ports. We consider a physical system where the high-index material has an instantaneous Kerr non-linearity (index change of $n_H c\varepsilon_0 n_2 |\boldsymbol{E}(x,y,t)|^2$, where n_2 is the Kerr coefficient). We neglect the Kerr effects in the low-index material. In order to simplify computations without sacrificing physics, we consider only the region within the square of ± 3 rods from the cavity to be non-linear. Essentially all of the energy of the resonant mode is within this square, so it is the only region where the non-linearity will have a significant effect.

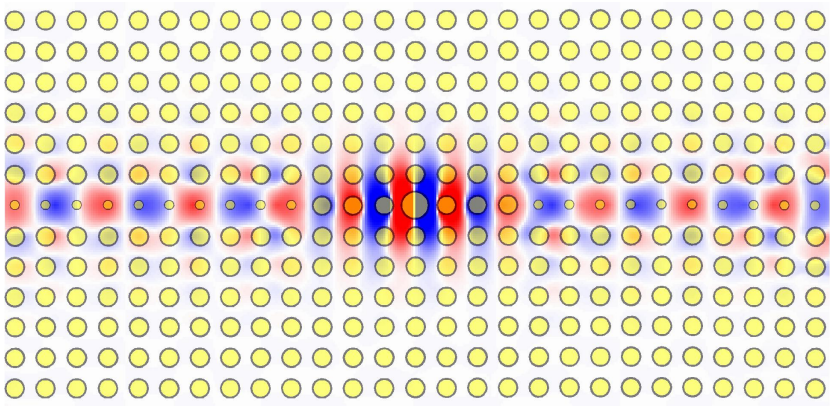

Figure 1: Electric field for a photonic crystal bistable switch at 100% resonant linear transmission. The device consists of a resonant cavity in a square lattice of high dielectric (non-linear) rods coupled (via tunneling effects) to two waveguides that serve as input and output ports.

Consider now numerical experiments to explore the behavior of the device. Namely, we solve the full 2D non-linear finite-difference time-domain (FDTD) equations [8], with perfectly matched layer (PML) boundary regions to simulate our system. The nature of these simulations is that they model Maxwell's equations *exactly*, except for the discretization; as one increases the numerical resolution, these simulations should asymptotically reproduce what is obtained in an experiment. Most of the simulations are performed at a resolution of *12*12* pixels per *a*a*; doubling the resolution changes the results by less than 1%. To match the waveguide modes inside the PC to the PML region, the PC waveguide is terminated with a distributed-Bragg reflector [9].

The system is designed so that it has a TM band gap of *18%* between $\omega_{MIN}=0.24(2\pi c)/a$, and $\omega_{MAX}=0.29(2\pi c)/a$. Furthermore, the single-mode waveguide created can guide all of the frequencies in the TM band gap. Finally, the cavity is designed to have a resonant frequency of $\omega_{RES}=0.2581(2\pi c)/a$ and a

*) Note that this is just one particular way of implementing line defects in PCs; a more common way to create a line defect would be to completely remove an entire line of rods.

Lorentzian transmission spectrum: $T(\omega) \equiv P_{OUT}(\omega)/P_{IN}(\omega) \approx \gamma^2/[\gamma^2+(\omega-\omega_{RES})^2]$, where P_{OUT} and P_{IN} are the outgoing and incoming powers respectively, and γ is the width of the resonance. The quality factor of the cavity is found to be $Q=\omega_{RES}/2\gamma=557$.

As a first numerical experiment, we launch off-resonance pulses whose envelope is Gaussian in time, with full-width at half-maximum (FWHM) $\Delta\omega/\omega_0=1/1595$, into the input waveguide. The carrier frequency of the pulses is $\omega_0=0.2573(2\pi c)/a$ so $\omega_{RES}-\omega_0=3.8\gamma$. When the peak power of the pulses is low, the total output-pulse energy ($E_{OUT} \equiv \int_{-\infty}^{\infty} dt P_{OUT}$) is only a small fraction (*6.5%*) of the incoming pulse energy E_{IN}, since we are operating off-resonance. As we increase the incoming pulse energy, the ratio E_{OUT}/E_{IN} increases, at first slowly. However, as we approach the value of $E_{IN}=(0.57*10^{-1})*(\lambda_0)^2/cn_2$(†), the ratio E_{OUT}/E_{IN} grows rapidly to *0.36*; after this point, E_{OUT}/E_{IN} slowly decreases as we increase E_{IN}. The dependence of E_{OUT}/E_{IN} vs E_{IN} is shown in Figure 2.

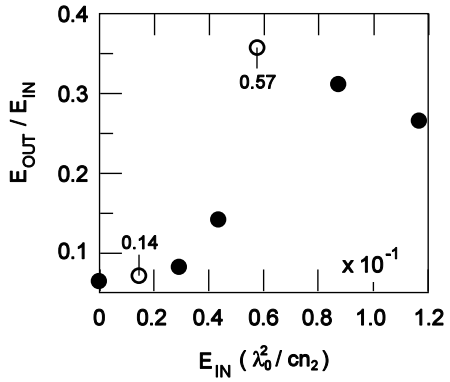

Figure 2: Transmission of Gaussian-envelope pulses through the device of Figure 1. As E_{IN} is increased, the E_{OUT}/E_{IN} ratio slowly grows. At a large enough E_{IN}, the ratio of the outgoing and incoming pulse energies increases sharply.

Intuitively, as one increases the optical power, the increasing index due to the non-linearity lowers ω_{RES} through ω_0, causing a rise and fall in transmission. This simple picture however is modified by non-linear feedback: as one moves into the resonance, coupling to the cavity is enhanced (positive feedback) creating a sharper on-transition and as one moves out of the resonance, the coupling is reduced (negative feedback) causing a more gradual off-transition.

Consider now a repetition of the above simulation, but with continuous-wave (CW) signals launched into the cavity instead of Gaussian pulses. There are two reasons for doing this. First, the upper branch of the expected hysteresis curve is difficult to probe using only a single input pulse. Second, it is much simpler to construct an analytical theory explaining the phenomena when CW signals are used. In all cases, we find that the amplitudes of the input signals grow slowly (compared with the cavity decay time) from zero to some final CW steady state values. Denoting by P_{IN}^S, P_{OUT}^S the steady-state values of P_{IN} and P_{OUT} respectively, we obtain the results shown by circles in Figure 3. For low P_{IN}^S, P_{OUT}^S slowly increases with increasing P_{IN}^S. However, at a certain P_{IN}^S, P_{OUT}^S jumps discontinuously. This is precisely the desired performance, but it is not the full story.

Hysteresis loops occur quite commonly in systems that exhibit optical bistability; an upper hysteresis branch is the physical manifestation of the fact that the system "remembers" that it had a high P_{OUT}/P_{IN} value previous to getting to the current value. To observe the upper hysteresis branch, we launch pulses that are superpositions of CW signals and Gaussian pulses (where the peak of the Gaussian pulse is significantly higher than the CW steady state value). In this way the Gaussian pulse will "trigger" the device into a high

†) Here, λ_0 is the carrier wavelength in vacuum.

P_{OUT}/P_{IN} state and, as the P_{IN} relaxes into its (lower) CW value, the P_{OUT} will eventually reach a steady state point on the upper hysteresis branch. This is confirmed in Figure 3 where we plot P_{OUT}^S as dots. After the CW value of P_{IN}^S passes the threshold of the upper hysteresis branch, the P_{OUT}^S value is always on the upper hysteresis branch.

For the case of CW signals, one can achieve a precise analytical understanding of the phenomena observed. In particular, we demonstrate below that there is a single additional fundamental physical quantity associated with this cavity (in addition to Q and ω_{RES}) that allows one to fully predict the $P_{OUT}^S(P_{IN}^S)$ behavior of the system. First, according to first-order perturbation theory, the field of the resonant mode will (through the Kerr effect) induce a change in the resonant frequency of the mode, given by:

$$\frac{\delta\omega}{\omega_{RES}} = -\frac{1}{4} * \frac{\int_{VOL} d^d \boldsymbol{r} \left[\left| \boldsymbol{E}(\boldsymbol{r}) \cdot \boldsymbol{E}(\boldsymbol{r}) \right|^2 + 2 \left| \boldsymbol{E}(\boldsymbol{r}) \cdot \boldsymbol{E}^*(\boldsymbol{r}) \right|^2 \right] n^2(\boldsymbol{r}) n_2(\boldsymbol{r}) c\varepsilon_0}{\int_{VOL} d^d \boldsymbol{r} \left| \boldsymbol{E}(\boldsymbol{r}) \right|^2 n^2(\boldsymbol{r})} \tag{1}$$

where $n(\boldsymbol{r})$ is the unperturbed index of refraction, $\boldsymbol{E}(\boldsymbol{r},t) = [\boldsymbol{E}(\boldsymbol{r})\exp(i\omega t) + \boldsymbol{E}^*(\boldsymbol{r})\exp(-i\omega t)]/2$ is the electric field, $n_2(\boldsymbol{r})$ is the local Kerr coefficient, $c\varepsilon_0 n_2(\boldsymbol{r}) n(\boldsymbol{r}) |\boldsymbol{E}(\boldsymbol{r})|^2 \equiv \delta n(\boldsymbol{r})$ is the local non-linear index change, VOL of integration is over the extent of the mode, and d is the dimensionality of our system. We now introduce a new dimensionless and scale-invariant parameter κ, defined as:

$$\kappa \equiv \left(\frac{c}{\omega_{RES}} \right)^d * \frac{\int_{VOL} d^d \boldsymbol{r} \left[\left| \boldsymbol{E}(\boldsymbol{r}) \cdot \boldsymbol{E}(\boldsymbol{r}) \right|^2 + 2 \left| \boldsymbol{E}(\boldsymbol{r}) \cdot \boldsymbol{E}^*(\boldsymbol{r}) \right|^2 \right] n^2(\boldsymbol{r}) n_2(\boldsymbol{r})}{\left[\int_{VOL} d^d \boldsymbol{r} \left| \boldsymbol{E}(\boldsymbol{r}) \right|^2 n^2(\boldsymbol{r}) \right]^2 n_2(\boldsymbol{r})\big|_{MAX}}, \tag{2}$$

As we shall see below, κ is a measure of the geometric non-linear feedback efficiency of the system. We thus call κ the *non-linear feedback parameter*. κ is determined by the degree of spatial confinement of the field in the non-linear material; it is a very weak function of everything else. κ is scale invariant because of the factor $(c/\omega_{RES})^d$, and is independent of the material n_2 because of the factor $n_2(\boldsymbol{r})|_{MAX}$ (the maximum value of $n_2(\boldsymbol{r})$ anywhere). Because the change in the field pattern of the mode due to the nonlinear effects (or due to small deviations from the operating frequency) is negligible, κ will also be independent of the peak amplitude. Moreover, since the spatial extent of the mode changes negligibly with a change in the Q of the cavity, κ is independent of Q. We found this to be true within 1% for cavity with Q=557, 2190, and 10330 (corresponding respectively to 3,4, and 5 unperturbed rods comprising the walls.) Indeed we find $\kappa = 0.195 \pm 0.006$ across all the simulations in this work, regardless of input power, Q, and operating frequency. (For comparison, if one had a system in which all the energy of the mode were contained uniformly inside a volume $(\lambda_0/2n_H)^3$, κ would be ≈0.34.) Thus, κ is an independent design parameter. The larger the κ, the more efficient the system is. Moreover, κ facilitates system design since a single simulation is enough to determine it. One can then add rods to get the desired Q, and change the operating frequency ω_0 until one gets the desired properties.

Let us now construct an analytical model to predict the non-linear response of a cavity in terms of only three fundamental quantities: the resonance frequency ω_{RES}, the quality factor Q, and the nonlinear feedback parameter κ. From Equations (1) and (2), we get $\delta\omega = -(1/2)(\omega_{RES}/c)^d \kappa Q c P_{OUT}^S n_2(\boldsymbol{r})|_{MAX}$; to see this note that the integral in the denominator of those equations is proportional to the energy stored in the cavity, which is in turn proportional to QP_{OUT}^S. Next, a Lorentzian resonant transmission gives $P_{OUT}^S/P_{IN}^S = \gamma^2/[\gamma^2 + (\omega_0 - \delta\omega - \omega_{RES})^2]$. This expression can be simplified by defining two useful quantities: $\delta = (\omega_{RES} - \omega_0)/\gamma$, the relative detuning of the carrier frequency from the resonance frequency, and

$P_0 \equiv \dfrac{1}{\kappa Q^2 \left(\omega_{RES}/c\right)^{d-1} n_2(\mathbf{r})\big|_{MAX}}$, a "characteristic power" of the cavity. With these definitions the relation between P_{OUT}^S and P_{IN}^S becomes:

$$\frac{P_{OUT}^S}{P_{IN}^S} = \frac{1}{1+\left(P_{OUT}^S/P_0 - \delta\right)^2}. \qquad (3)$$

Thus, $P_{OUT}^S(P_{IN}^S)$ is now reduced to depend on only two parameters, P_0 and δ, each one of them having separate effects: a change in P_0 is equivalent to a rescaling of both axes by the same factor, while the shape of the curve can only be modified by changing δ. In general, cubic equation (3) can have either one or three real solutions for P_{OUT}^S, depending on the value of the detuning parameter δ. The bistable regime corresponds to three real solutions and requires a detuning parameter $\delta > \sqrt{3}$. As mentioned earlier the detuning in our simulations is $\omega_{RES}-\omega_0=3.8\gamma$, which means that δ = 3.8, well within the predicted bistability regime. Equation (3) is plotted in Figure 3 as a line for the case of $Q=557$ and $\kappa=0.195$. It is in excellent agreement with the results from the computational experiments, predicting both the upper and lower hysteresis branches exactly. Note that the middle branch (dashed green line) is unstable in that tiny perturbations cause the solution to decay to either the upper, or lower branch [10].

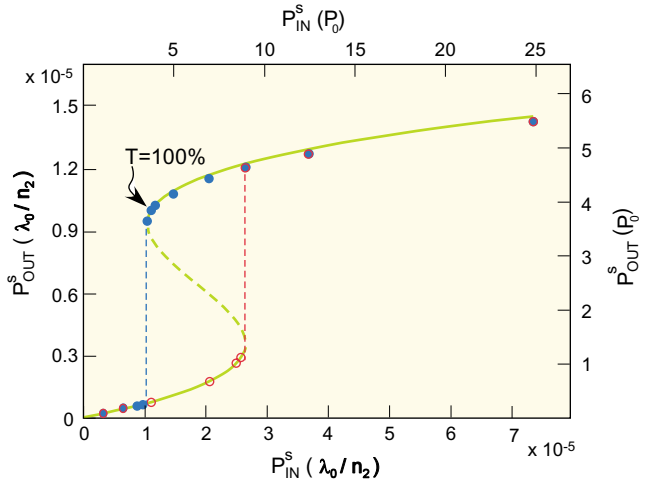

Figure 3: Plot of P_{OUT}^S vs. P_{IN}^S for the device of Figure 1. The circles are obtained by launching CW signals into the device. The dots correspond to launching superpositions of Gaussian pulses and CW signals into the cavity in order to access the hysteresis portion of the curve. The line is the analytical prediction, corresponding to $\delta=3.8$ and $P_0=2.6*10^{-6}\lambda_0/n_2$.

From Eq. (3) one can also calculate some typical power levels for the device. For example, the input power needed for 100% transmission can be seen to be $P_{100\%} = \delta P_0$ (corresponding to $P_{IN}^S=3.8P_0$ in Figure 3.) The minimum power needed for bistability is attained when $\delta = \sqrt{3}$ in which case we obtain

$$P_{b,\min} = \sqrt{3}P_0 = \frac{\sqrt{3}}{\kappa Q^2 \left(\omega_{RES}/c\right)^{d-1} n_2(\mathbf{r})\big|_{MAX}}.$$

Since the profiles of our modes are so similar to the cross-sections of the 3D modes described in Ref 7, we can use our 2D simulations to estimate the power needed to operate a true 3D device. According to what is shown in Ref 7, we are safe to assume that in a 3D device, the profile of the mode at different positions in the 3rd dimension will be roughly the same as the profile of the mode in the transverse direction of the 2D system. Thus, taking the Kerr coefficient to be $n_2=1.5*10^{-17}m^2/W$, (a value achievable in many nearly-instantaneous non-linear materials), and a carrier wavelength $\lambda_0=1.55\mu m$, gives a characteristic power of $P_0=77mW$, and a minimum power to observe bistability of $P_{b,min}=133mW$.

This level of power is many orders of magnitude lower than that required by other small all-optical ultra-fast switches! There are two reasons for this. First, the transverse area of the modes in the photonic crystal in question is only $\approx(\lambda/5)^2$; consequently, to achieve the same-size non-linear effects (which depend on intensity), we need much less power than in other systems that have larger transverse modal area. Second, since we are dealing with a highly confined, high-Q cavity, the field inside the cavity is much larger than the field outside the cavity; this happens because of energy accumulation in the cavity. In fact, from the expression for the characteristic power P_0, one can see that the operating power falls as $1/Q^2$. Building a high-Q cavity that is also highly confined is very difficult in systems other than photonic crystals, so we expect high-Q cavities in photonic crystals to be nearly optimal systems with respect to the power required for optical bistability. For example, a Q=4000 would be quite useful for telecommunications, and leads to the operational power of roughly 2.6mW. Moreover, the peak $\delta n/n$ needed to operate the device would be 0.001, which is definitely possible with conventional instantaneous Kerr materials. Consequently, the response and recovery time could easily be smaller than 1ps. Potential applications for such a device include: optical logical gates, switches, optical regeneration, all-optical memory, and amplification [10].

3. OPTICAL BISTABILITY IN AXIALLY MODULATED OMNIGUIDE FIBERS

OmniGuide fibers are a new type of cylindrical multi-layer dielectric fibers [11] that have only very recently been implemented experimentally [12]. Their cladding is an omni-directional multi-layer mirror that reflects light of any polarization and any direction. These photonic bandgap fibers can have a hollow core and a guiding mechanism that depends only on the cladding. We propose to exploit these facts to obtain much stronger axial optical modulation than is possible in conventional fibers through insertion of material (e.g. spheres) into the core. Moreover, due to strong transverse confinement, much smaller transverse modal areas are possible than in usual low index-contrast fibers. In this way, we show how optimal ultra-fast bistable devices can be achieved with operating powers less than *40mW*, whose highly nonlinear input/output power relation is key to many applications [10] (e.g. all-optical pulse reshaping, optical limiting, logic gates, etc.). Our device retains all the advantages of similar photonic crystal (c.f. Section 2) or high index-contrast devices [13] in terms of power, size, and speed. On the other hand, the fact that it is an in-fiber device should make it easier to produce and to couple with another fiber. We solve the full non-linear Maxwell's equations numerically to demonstrate optical bistability in this class of systems. Moreover, we present an analytical model that excellently describes their behavior and is very useful in predicting optimal designs.

A schematic of a typical design is shown in Figure 4. It consists of an axially modulated single-mode OmniGuide fiber with a core of diameter $0.41\lambda_0$, where λ_0 is the carrier wavelength in vacuum. The cladding consists of 7 bilayers (periods), each $0.3\lambda_0$ thick, 30% of which thickness is the high index (n_H=2.8) material. The inner-most layer, adjacent to the core, is low-index (n_L=1.5). The axial modulation consists of 41 (n_{SPH}=1.5) spheres tightly filling the core (diameter $0.41\lambda_0$). The periodicity of the axial modulation opens a bandgap for the propagating mode. Our 3D frequency-domain simulations [14] tell us that structures like the one in Figure 1 easily open axial bandgaps of *6%* or larger (vs. *<0.1%* in grated silica fibers).

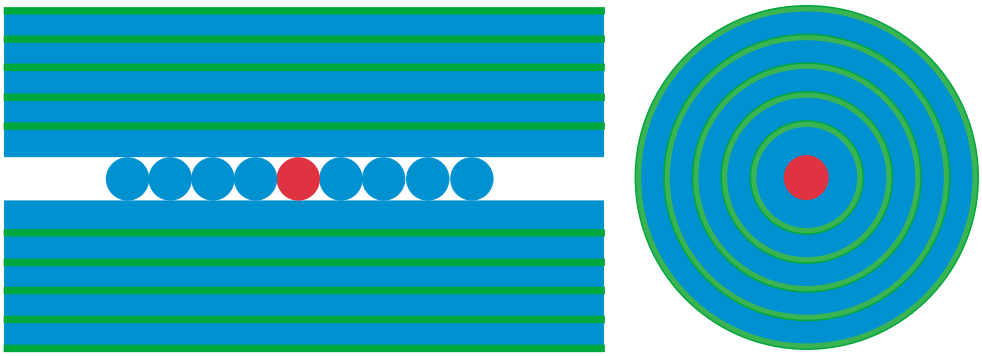

Figure 4: Schematic of a non-linear OmniGuide device in which we demonstrate optical bistability. The left panel presents a longitudinal cross-section; the panel on the right presents a transverse cross-section.

A defect in the axial periodicity creates a resonant cavity supporting a tightly confined, high-Q resonant mode. In the implementation of Figure 4, the defect is introduced by changing the index of refraction of the central sphere to n_{DEF}=1.9. Tight confinement in the transverse direction is provided by the large band-gap of the OmniGuide cladding, while strong confinement in the axial direction is provided by the large axial bandgap. The cavity couples to the waveguide (axially uniform fiber) through tunneling processes. We model the low-index material to have an instantaneous Kerr non-linearity (the index change is $\delta n(\mathbf{r},t)=cn_L\varepsilon_0 n_2|\mathbf{E}(\mathbf{r},t)|^2$, where n_2 is the Kerr coefficient.)

We perform nonlinear finite-difference time-domain (FDTD) simulations [8], with perfectly matched layers (PML) boundary condition, of this system. Due to the cylindrical symmetry of the system in Figure 4, our system is effectively two-dimensional. Consequently, we can obtain excellent physical understanding of the system by performing 2D FDTD simulations. The numerical values obtained with 2D calculations will differ from the true 3D values only by a geometrical factor of order unity.

The cavity supports a strongly localized resonant mode (transverse modal area $\approx \lambda^2/3$ and axial length of the mode $\approx 6\lambda_0$). The system has a nearly Lorentzian transmission spectrum: $T(\omega)\equiv P_{OUT}(\omega)/P_{IN}(\omega) \approx \gamma_W^2/[(\gamma_R\gamma_W^2+(\omega-\omega_{RES})^2]$, where P_{OUT} and P_{IN} are the outgoing and incoming powers respectively, ω_{RES} is the resonant frequency, γ_W is the decay width due to the coupling of the cavity mode to the waveguides, while γ_R is the decay width due to the coupling to the cladding modes [15]. We measure a quality factor $Q=\omega_{RES}/[2(\gamma_R+\gamma_W]=540$, and a peak transmission $T_P=0.88$; from this we obtain that the radiation quality factor $Q_R=\omega_{RES}/2\gamma_R=8700$. Q_R is finite due to the coupling of energy to the radiating cladding modes; this coupling is the primary cause of losses in our system, but can be controlled [16].

First, we perform numerical experiments in which we launch a series of Gaussian pulses into the system. We choose a carrier frequency $\omega_0=\omega_{RES}-3.2(\gamma_W\gamma_R)$, and the full-width half-maximum (FWHM) bandwidth of our pulses is $\omega_0/FWHM$ = 796. The ratio of the transmitted (E_{OUT}) vs. incoming (E_{IN}) pulse energy increases sharply as we approach the bistability threshold, and decreases after the threshold is passed, as shown in the upper-left panel of Figure 5. Transmitted pulse spectra are also shown for a few pulses in upper-right panel of Figure 5; the non-linear cavity redistributes the energy in the frequency spectrum; if these changes to the spectrum are undesirable, they can be removed by: optimizing the device, using time-integrating non-linearity, or by adding a frequency-dependent filter to the output of the device. Typical output-pulse shapes are shown in the lower panels of Figure 5. As one can see in the lower-left panel, even without optimizing our system, we still obtain well-behaved shapes of output pulses in the regime where E_{OUT}/E_{IN} is maximal.

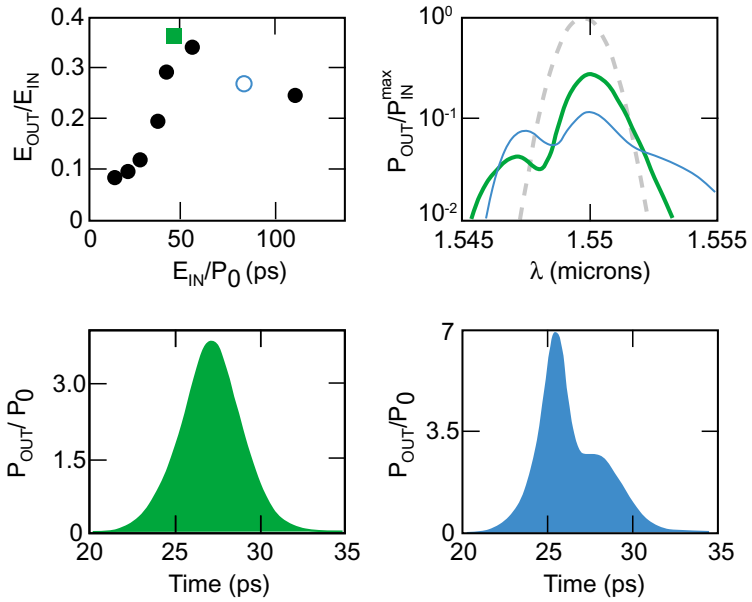

Figure 5: Numerical experiments with launching temporal-Gaussian pulses into the non-linear system of Figure 4. The upper-left panel shows the transmission as a function of the incoming pulse energy. The lines in the upper-right panel display the output spectra for a few pulses; the spectrum of each pulse is normalized to its peak incoming power (i.e. the input pulse, normalized in the same manner is displayed with the dashed line). The lower panels show the output shapes for a few incoming pulses. The square in the upper-left panel corresponds to the thick solid line in upper-right panel, and to the pulse in the lower-left panel. The circle in the upper-left panel corresponds to the thin solid line in the upper-right panel, and to the pulse in the lower-right panel.

For the case of CW signals we can achieve a precise analytical understanding of bistability in this system, making use of the non-linear feedback parameter κ: Let us denote by P_{IN}^S, P_{OUT}^S the steady-state values of P_{IN} and P_{OUT} respectively. Using a Lorentzian transmission spectrum in the linear case and perturbation theory for small $\delta n(\mathbf{r})$, we obtain:

$$\frac{P_{OUT}^S}{P_{IN}^S} = \frac{T_P}{1+\left(P_{OUT}^S/P_0 - \delta\right)^2}, \tag{4}$$

where $\delta=(\omega_{RES}-\omega_0)/(\gamma_W+\gamma_R)$, $T_P=[\gamma_W^2/(\gamma_W+\gamma_R)^2]$ is the peak transmission, and P_0 is a "characteristic power" of this cavity given by:

$$P_0 \equiv \frac{\sqrt{T_P}}{\kappa Q^2 \left(\omega_{RES}/c\right)^{d-1} n_2(\mathbf{r})\big|_{MAX}}, \tag{5}$$

where κ is given by Eq.(2). According to Eq.(4), P_0 sets the power scale for observing bistability in a cavity of interest.

To check our analytical theory, we obtain $\kappa=0.020$ from a single non-linear computation; together with the knowledge of Q and ω_{RES}, we obtain $P_{OUT}^S(P_{IN}^S)$ for $\delta=3.2$ which we plot, as a solid line in Figure 6. We compare our analytical theory with numerical experiments in which we launch smoothly turned-on CW signals into the cavity. To observe the upper hysteresis branch we launch large-amplitude and wide-width Gaussian pulses that decay into smaller steady state CW values. The small discrepancy between our

analytical theory and the numerical experiments in Figure 6 is mostly attributable to the fact that the linear-regime transmission curve is not a perfect Lorentzian.

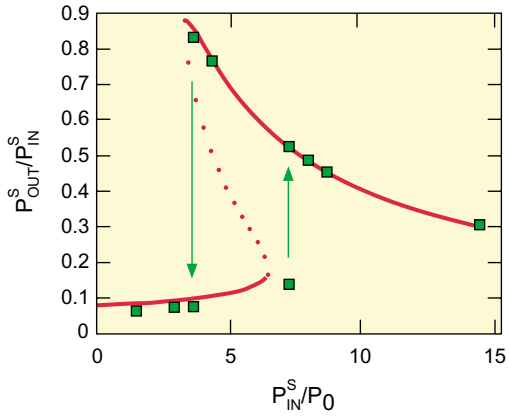

Figure 6: Plot of the observed P_{OUT}^{S} vs. P_{IN}^{S} for the device from Figure 4, when $\delta=3.2$. The squares are points obtained from numerical experiments. The line is the analytical prediction, which clearly matches the numerical experiments; the dotted part of the line is unstable and therefore physically unobservable.

While numerical simulations for larger *Q*s would be prohibitively long, our analytical model allows us to predict the behavior of a high-Q device. According to Eq.(5), the power requirements drop with $1/Q^2$. *Q* can be increased by adding more spheres to the "walls" of the cavity. For *Q* of *6000* (which is still compatible with *10Gbit/sec* signals), the non-linear index changes are *<0.001* (which is still compatible with nearly instantaneous non-linear materials). The power needed to observe bistability is *34mW* (assuming $n_2=1.5*10^{-17}m^2/W$, a value typical for the materials we are using), which is fairly close to the *5mW* single-channel peak power levels used in telecommunications. The power can be further decreased by reducing the modal volume and/or by using materials with larger Kerr coefficient.

There are two reasons why the required power is so small compared to other fiber systems that display optical bistability [17,18]. First, all the energy of the mode is concentrated in a very small modal volume; consequently, for the same amount of modal energy, the peak $\delta n(\mathbf{r})$ induced in the system is much larger than in other systems with much larger modal volumes [18]. This is manifested by the fact that the non-linear feedback parameter $\kappa=0.020$ is fairly large. (For comparison, if one had a system in which all the energy of the mode were contained uniformly inside a volume $(\lambda_0/2n_L)^3$, κ would be ≈0.15.) Second, a large quality factor can be achieved at the same time as the large κ: Increasing *Q* while keeping other parameters fixed decreases the power requirements as $1/Q^2$ [19]. The first factor of *Q* appears because increasing *Q* for a fixed P_{IN} leads to a larger peak electric field inside the cavity, due to the longer energy accumulation. The second factor of *Q* comes from the fact that the resonance peak width is *~1/Q*, thereby reducing the required frequency (index) shift by *1/Q* as well.

On the experimental front, so far we have been successful in inserting $d=1.75\mu m$ spheres into $d=2\mu m$ core fiber via capilary action (optical tweezers could be used instead) [20]. To our advantage, spheres tend to stick together due to Van der Vaals forces. As a next step, we plan to decrease the pressure inside the core, and heat the fiber to the melting point, so it would clasp tightly onto the spheres; this is a standard technique usually used to decrease the core radii of hollow-core fibers. Clearly, there are many other possibilities for implementing the axial modulation. Conceptually, the fact that the guiding mechanism does not depend on the core and the fact that the core is initially hollow, provide for significantly more experimental flexibility in implementing a strong optical axial modulation than exists in conventional fibers. Other authors [21] demonstrated impressive manipulation of optical properties of holey fibers by inserting various kinds of materials into the holes, including producing periodic axial modulation of the core. Alternatively, one could perform photo-litography on the inner surface of the core: a photoresist would be co-

drawn as the inner-most layer of the cladding, laser beams shone from the side would implement cross-linking of the photo-resist, and then the hollow core would be used to transport all the acids and/or bases needed to etch a periodic structure onto the inner-most layer of the cladding.

We would like to emphasize that since the transverse confinement principle is not index guiding, periodic axial modulation is not the only way to achieve axial confinement in OmniGuide fibers. In fact, simply shrinking the core radius [21] (or equivalently decreasing the index of the core) of an OmniGuide fiber can shift the cutoff frequency of the operating mode above the operating frequency—similarly to a metallic waveguide, a mode experiences an exponential decay once it encounters such a region; this property is sufficient to implement all the ideas presented above. Finally, one should be able to implement all the principles described in this manuscript in any hollow photonic crystal fiber that has a large enough lateral bandgap.

4. BISTABILITY IN DOUBLE-DEFECT PHOTONIC CRYSTAL SYSTEMS

In this Section, we describe a novel device system with 4 ports that provides very important new performance characteristics. For example, essentially no portion of the incoming pulse is ever reflected back into the input waveguide. Having zero reflection is of crucial importance for integration with other active devices on the same chip. Through the use of analytical theory, and detailed numerical simulations, we explain this device's underlying physics and demonstrate its operation as an all-optical transistor and for optical isolation.

Ideally, for many applications one would like to have a device with two inputs whose output has a strong dependence on the (weak) amplitude of one of its inputs (the probe input). Moreover, for ultimate efficiency, one would require single-mode waveguiding, high-Q cavities, and controllable radiation losses. A non-linear PC system can provide us with all of these capabilities.

The system we propose is shown in Figure 7. It is reminiscent of the channel-drop filter introduced in Ref. 22. The critical difference is that the PC is now made of high index non-linear rods suspended in air, and this leads to important new functionality. The rods are made from an instantaneous Kerr material with index change of $nc\varepsilon_0 n_2|\boldsymbol{E}(x,y,t)|^2$, where n_2 is the Kerr coefficient. The system consists of two waveguides, and two single-mode high-Q resonant cavities. The even, and odd states supported by the two-cavity system are designed to be degenerate both in their resonant frequencies, and also in their decay times. Signals propagating rightwards couple only to a particular superposition of the two states that in turn decays only into rightwards propagating signals; consequently, there is never any reflection back into leftwards direction. Since the energies stored in the two cavities are always equal, presence of the non-linearity does not spoil the required left-right symmetry of the system(‡). Consequently, to the lowest order, the influence of the non-linearity is only to change the doubly-degenerate resonant frequency ω_{RES} depending on the intensity of the signal. For a weak CW signal at ω, applied at port (1), the output at port (4) is given by: $T_4(\omega)\equiv P_{OUT4}(\omega)/P_{IN1}(\omega)=\gamma^2/[\gamma^2+(\omega-\omega_{RES})^2]$, where P_{OUT4} and P_{IN1} are the outgoing and incoming powers respectively, and γ is the width of the resonance; the output at (2) is given by: $T_2(\omega)=1-T_4(\omega)$, while the outputs at (1)&(3) are zero for all frequencies, because of the degeneracy and chosen symmetries of the two resonant modes.

‡) One might wonder whether it is possible to excite states of the system that are not left-right symmetric. We were able to excite such states with certain initial conditions that purposely ruined the left-right symmetry of the system, and in fact some of these states seemed to be stable. Nevertheless, the states that have left-right symmetry appear to be particularly stable; various non-linearly induced left-right asymmetries (at typical operating power levels) with as big as 10% difference in the energies stored in the two cavities did not seem to destabilize them.

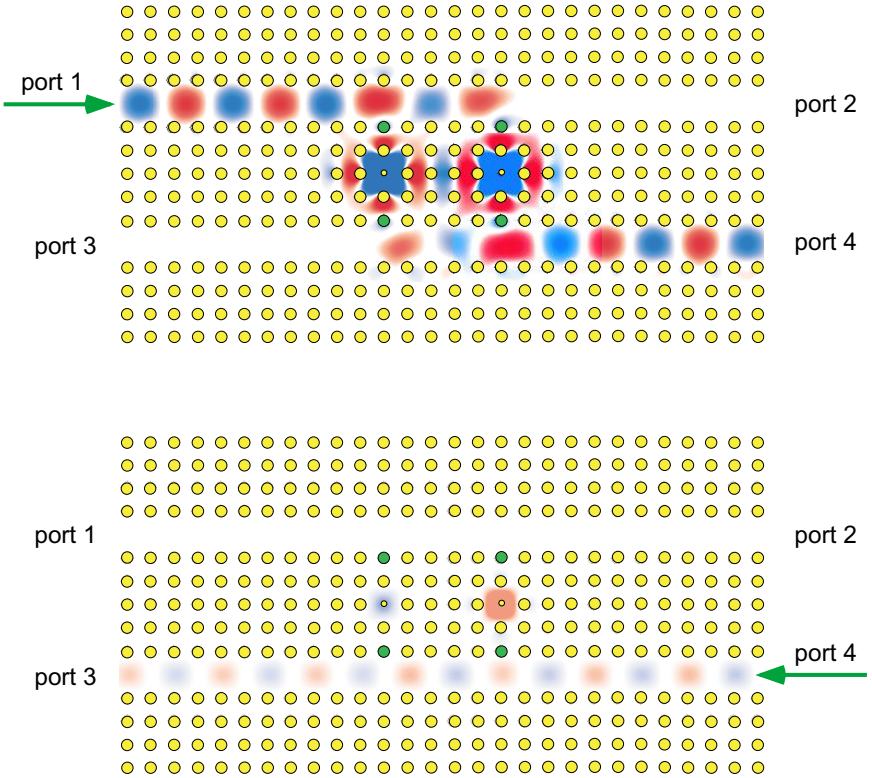

Figure 7: Basic 4-port non-linear PC device that we use to demonstrate optical bistability. The PC consists of high-index $\varepsilon_H=11.56$ rods with radius $0.2a$, a being the lattice constant. The four differently colored rods in each plot have $\varepsilon=9.5$; the small rods have $\varepsilon=6.2$, and radius of $0.05a$. As an example of the use of the device, we show the electrical fields in the case when it performs optical isolation. Top shows a strong forward-propagating pulse. Bottom shows a weak reflected backward-propagating pulse. We model the high index rods as having an instantaneous Kerr non-linearity.

Given these forms for the transmission, we can follow the framework of Section 2 to predict that the system will exhibit optical bistability if the carrier frequency ω_0 is sufficiently below the resonant frequency: $\delta \equiv (\omega_{RES} - \omega_0)/\gamma > \sqrt{3}$. Using the analytical framework of Section 2, the steady state values of the CW powers of interest are: $\frac{P^S_{OUT4}}{P^S_{IN1}} = \frac{1}{1+\left(P^S_{OUT4}/P_0 - \delta\right)^2}$, and $P_{OUT2}{}^S/P_{IN1}{}^S = 1 - P_{OUT4}{}^S/P_{IN1}{}^S$, where "characteristic power", $P_0 \equiv \frac{1}{\kappa Q^2 (\omega_{RES}/c) n_2(\boldsymbol{r})|_{MAX}}$. We establish that for the current system the non-linear feedback parameter $\kappa=0.11$, while the quality factor is $Q=\omega_{RES}/2\gamma=730$. For definiteness, we take $\delta=4.25$, so bistability should be easily observable. We plot the analytical prediction as the green line in Figure 8; the dashed portion of that line is unstable, and thereby physically unobservable.

To verify this simple and powerful prediction, we perform numerical experiments (non-linear finite-difference time-domain (FDTD) simulations with perfectly matched layers (PML) boundary conditions) on this system. The current work, and the work of Ref. 22, are for a 2D model; this decreases numerical requirements on our simulations significantly compared to 3D simulations. Nevertheless, it has been shown

recently [7] that one can find an equivalent 3D system that will behave qualitatively the same, while the quantitative differences will be only of a geometrical factor close to 1.

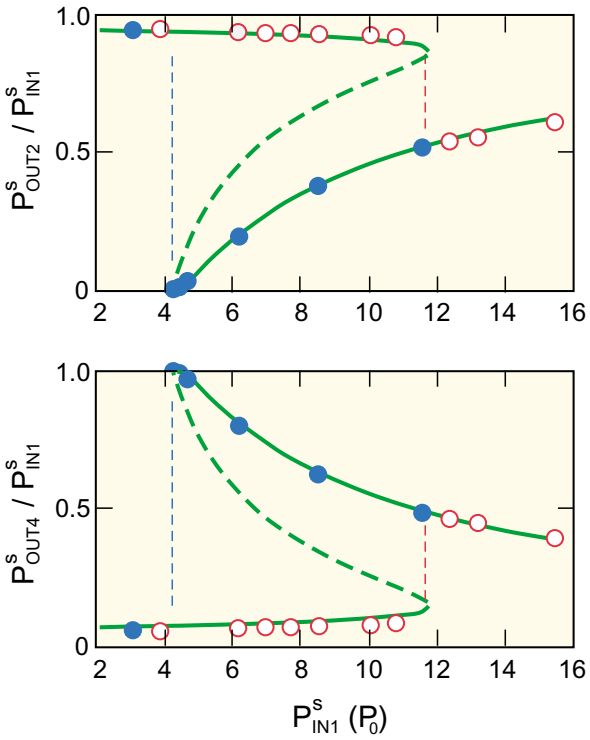

Figure 8: Plots of the observed $T \equiv P_{OUT}{}^S / P_{IN}{}^S$ vs. $P_{IN}{}^S$ for the device from Figure 7. The upper panel shows the power observed at output (2), while the lower panel shows the power observed at output (4). The input signal enters the device at port (1). The circles are points obtained by launching CW signals into our device. The dots are measurements that one observes when launching superpositions of Gaussian pulses and CW signals into the system. The lines are from an analytical model described in the text.

To observe the lower bistability hysteresis branch, we send smooth CW signals into the port (1) of the system, and we vary the peak power of the incoming signals. In order to observe the upper bistability hysteresis branch, we launch superpositions of wide Gaussian pulses that decay into smaller-intensity CW signals, thereby relaxing into the points on the upper hysteresis branch. As shown in Figure 8, this device indeed displays optical bistability, and our analytical model is a very good representation of the physical reality. Throughout all of these simulations, the observed reflections back into ports (1)&(3) are always less than 1% of the incoming signal's power.

Given that the modes of the 2D system are so similar to the cross-sections of the modes described in Ref.7, we can use the 2D results, together with the analytical model of the system to predict the performance of the device in a real physical setting. According to Ref.7, once this device is implemented in a PC with complete 3D bandgap, the 3rd dimension extent of all the modes will be roughly $\lambda/3$. Let us assume that the Kerr coefficient of the material we are using is $n_2=1.5*10^{-17} m^2/W$, (a value achievable in many nearly-instantaneous non-linear materials, e.g. GaAs). Assuming a device with $Q=4000$ (which is still compatible with *10Gbit/s* signals), and carrier wavelength $\lambda_0=1.55\mu m$, we get that the characteristic power of the device is $P_0 \approx 5mW$, while the peak operating power needed to observe bistability is roughly *8mW.* (Compare this to the *5mW* peak power levels used in telecommunications today). The peak non-linearly induced $\delta n/n<0.001$, which is compatible with using nearly-instantaneous non-linear materials.

Let us now examine how we would use such a device for optical isolation. One of the biggest obstacles in achieving large-scale optics integration today is the non-existence of integrated optical isolators; active and non-linear devices typically do not tolerate small reflections coming from other devices they are integrated with. The most common approach involves breaking the time-reversal symmetry using magneto-optic materials; other approaches involve breaking backward-forward symmetry using non-linear materials [23]. Unfortunately, none of these approaches satisfy all the requirements mentioned earlier which are necessary for large-scale optics integration. The device of Figure 7 can perform integrated-optics isolation, for most applications of interest, eg. where the strength of each logical (forward-propagating) signal in a particular waveguide is above the bistability threshold, and the reflected (backward-propagating) signals are weak. An example of such operation is shown in Figure 7. A strong forward-propagating signal (operating at a high-transmission point of the bistability curve) is nearly perfectly transferred from port (1) to port (4). However, when a weak reflected signal (operating at a low-transmission point of the bistability curve) enters port (4) of the device at a later time, it proceeds to port (3), from where it can be discarded.

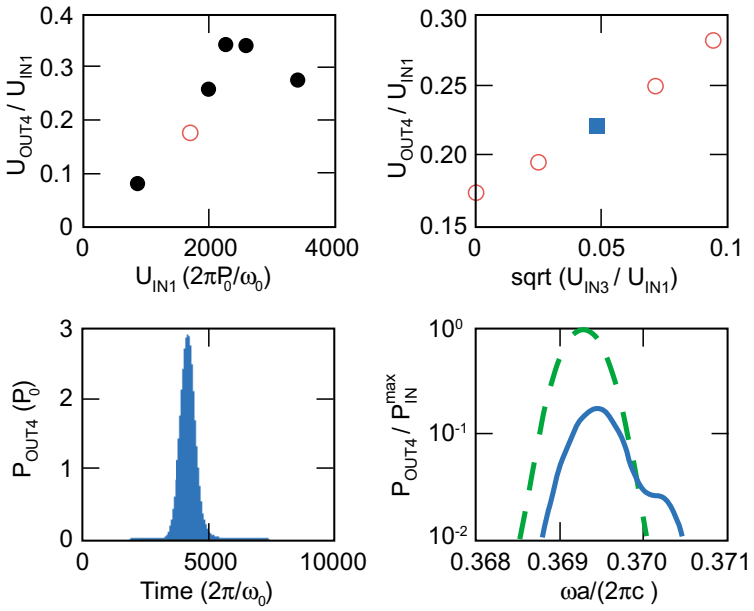

Figure 9: Results of launching Gaussian pulses into the device of Figure 7. Upper-left panel shows the observations of launching various energy (otherwise equal) pulses only into port (1). Upper-right panel shows the observations of launching a fixed signal (given by the circle from the upper-left panel) into the port (1) of the device, in parallel with launching various amplitude (otherwise equal) pulses into port (3). The lower-left panel, and the solid curve in the lower-right panel correspond to the pulse observed at port (4) when a signal (square in upper-right panel) is launched into the device. The lower-right panel also shows (in dashed line) the incoming pulse (both pulses in this panel are normalized to the peak power of the incoming pulse).

In real practical applications, one will typically be launching pulses into the device, rather than CW signals. Consequently, we also investigate what happens in this case. When the pulse duration is very long, the response is of course very similar to that of the CW case, following the circle-curve in Figure 8. As the pulse duration decreases, we expect the features of this transmission curve to smoothen-out. To check this, we perform a series of numerical experiments in which we launch various energy Gaussian pulses of carrier frequency $\omega_0=\omega_{RES}-4.25\gamma$, and full-width half-maximum (FWHM) bandwidth $\omega_0/FWHM=638$ into port (1) of the device. The ratio of the energy transmitted to port (4) is shown in the upper-left panel of Figure 9. The shape of this curve can also be intuitively understood as follows. As one increases the optical power, the increasing index due to the non-linearity lowers ω_{RES} through ω_0, causing a rise and fall in transmission. This simple picture however is modified by non-linear feedback: as one moves into the resonance, coupling to the cavity

is enhanced (positive feedback) creating a sharper on-transition and as one moves out of the resonance, the coupling is reduced (negative feedback) causing a more gradual off-transition.

As an illustration of another possible application of our device, we now exploit this sharper on-transition to construct an all-optical transistor. We perform a series of numerical experiments in which we launch into port (1) the pulses presented by the circle in the upper-left panel of Figure 9; however, in addition to this, we send identical (albeit smaller energy) pulses into port (3) of the system. We experimented with launching a few different energy pulses into (3); the results are shown in the upper-right panel of Figure 9. As we can see, the amplification can be quite drastic. Consider for example the square in that panel: the pulse sent into (3) had 0.25% of the energy of the pulse sent thru (1), resulting in an almost 5% increase in transmission to port (4); this implies an amplification of a factor of roughly 20. Such large amplifications are precisely the functionality one expects from an all-optical transistor (c.f. Section 2). An additional interesting feature of the upper-right panel of Figure 9, is that the energy observed at port (4) is essentially proportional to the square root of the energy sent in thru (3). This means that the energy amplification factor becomes infinite as the signal energy goes to zero, which may have some exciting new applications, such as a very low threshold laser. This behavior can be understood as follows. Pulses coming in thru (1)&(3) are coherent and in phase. Consequently, (taking into account the up-down symmetry of the system), once inside the cavities, the signals add in amplitude. Therefore, for small signals, and a given pulse incoming thru (1), the energy stored in the cavity is a linear function of the field applied at (3). Since the energy at (4) is a linear function of the energy stored in the cavities, it is a linear function of the square root of the energy coming thru (3). If instead we considered a time-integrating non-linearity, and temporally incoherent signals, for a fixed incoming pulse at (1), the energy output at (4) would be a linear function of the energy coming into (3) (in that case, the signals in the cavity would add in intensity, rather than in amplitude). Finally, since the frequency width of the pulses is comparable to the frequency width of the cavity, and the non-linear effects are quite extreme, it is important to determine possible distortions in the shapes of the output pulses. The use of FDTD simulations provides a bonus here, since a detailed description of output pulses is typically not feasible with other theoretical models. In general, we find that the output pulses retain their pulse shape, as shown in the lower panels of Figure 9.

With only minor modifications, the device system we propose can also be used for other applications [10], including: any all-optical logical gate, pulse reshaping and regeneration, noise-cleanup, optical diode [4], memory, etc. For any of these uses, when applying any signal to port (1) and/or port (3), one never has to worry about any reflections into ports (1) or (3). The control of reflections offered by devices of this type represents a low-power, ultra-fast, small-scale paradigm for implementing non-linear micro-devices in non-linear optics.

5. CONCLUSION

We demonstrated how unique opportunities of photonic crystals for molding the flow of light opened a new window of opportunity for using optical bistability for all-optical applications. Devices that can be designed using these principles are suitable for implementing large-scale optics integration, they are tiny in size, can be ultra-fast and operate with only a few mW of power.

We are especially grateful to Steve Jacobs, Torkel Engeness, Ori Weisberg and Maksim Skorobogatiy from OmniGuide Communications, Inc., for their help in developing the non-linear finite difference time domain code used in these simulations. We would also like to thank Prof. Moti Segev from Technion, and Prof. Erich Ippen of MIT for many useful discussions. This work was supported in part by the Materials Research Science and Engineering Center program of the National Science Foundation under Grant No. DMR-9400334.

REFERENCES

1 E. Yablonovitch, Phys. Rev. Lett. **58**, 2059 (1987).

2 S. John, Phys. Rev. Lett. **58**, 2486 (1987).

3 J. D. Joannopoulos, R. D. Meade, and J. N. Winn, *Photonic Crystals: Molding the flow of light* (Princeton University Press, Princeton, N.J., 1995).

4 S. F. Mingaleev, and Y. S. Kivshar, J. Opt. Soc. Am. B **19**, 2241 (2002).

5 E. Centeno, and D. Felbacq, Phys. Rev. B, **62**, R7683 (2000).

6 B. Xu, and N. Ming, Phys. Rev. Lett. **71**, 3959 (1993).

7 M. L. Povinelli, S. G. Johnson, S. Fan, and J. D. Joannopoulos, Phys. Rev. B **64**, 075313 (2001).

8 For a review, see A. Taflove, Computational Electrodynamics: The Finite-Difference Time-Domain Method (Artech House, Norwood, Mass., 1995).

9 A. Mekis, S. Fan, and J. D. Joannopoulos IEEE Microwave Guided Wave Lett. **9**, 502 (1999).

10 B. E. A. Saleh, and M. C. Teich, *Fundamentals Of Photonics* (John Wiley&Sons, 1991).

11 Y. Fink, D. J. Ripin, S. Fan, C. Chen, J. D. Joannopoulos, and E. L. Thomas, J. Lightwave Tech. **17**, 2039 (1999); Steven G. Johnson, Mihai Ibanescu, M. Skorobogatiy, Ori Weisberg, Torkel D. Engeness, Marin Soljačić, Steven A. Jacobs, J. D. Joannopoulos, and Yoel Fink, Optics Express, **9**, 748, (2001).

12 S.D.Hart, G.R.Maskaly, B.Temelkuran, P.H.Prideaux, J.D.Joannopoulos, Y.Fink, Science **296**, 511-513 (2002).

13 J.S.Foresi, P.R.Villeneuve, J.Ferrera, E.R.Thoen, G.Steinmeyer, S.Fan, J.D.Joannopoulos, L.C.Kimerling, H.I.Smith, and E.P.Ippen, Nature, **390**, 143, (1997).

14 Steven G. Johnson and J. D. Joannopoulos, Optics Express **8**, no. 3, 173-190 (2001).

15 See e.g. Shanhui Fan, Pierre R. Villeneuve, J.D.Joannopoulos, and H.A.Haus, Physical Review B, **64**, 245302, (2001), and H.A.Haus, *Waves And Fields in Optoelectronics* (Prentice-Hall, Englewood Cliffs, NJ, 1984).

16 S.G.Johnson, S.Fan, A.Mekis, and J.D.Joannopoulos, Applied Physics Letters, **78**, 3388 (2001).

17 S.Coen and M.Haelterman, Optics Letters, **24**, 80 (1999).

18 Stojan Radić, Nicholas George, and Govind P. Agrawal, JOSA B, **12**, 671 (1995).

19 A.Yariv, IEEE Photonics Technology Letters, **14**, 483, (2002), and J.E.Heebner, and R.Boyd, Optics Letters, **24**, 847 (1999).

20 Burak Temelkuran, personal communication.

21 C.Kerbage, and B.J.Eggleton, Optics&Photonics News, 38, September 2002.

22 S.Fan, P.R.Villeneuve, J.D.Joannopoulos, and H.A.Haus, Phys. Rev. Lett. **80**, 960 (1998).

23 M.Scalora, J.P.Dowling, M.J.Bloemer, and C.M.Bowden, Journal of Applied Physics **76**, 2023 (1994); K. Gallo, G. Assanto, K. R. Parameswaran, and M. M. Fejer, Appl. Phys. Lett. **79**, 314 (2001)